JGR Earth Surface

RESEARCH ARTICLE
10.1029/2021JF006576

Infrasonic and Seismic Analysis of Debris-Flow Events at Illgraben (Switzerland): Relating Signal Features to Flow Parameters and to the Seismo-Acoustic Source Mechanism

Giacomo Belli[1], Fabian Walter[2], Brian McArdell[2], Duccio Gheri[1], and Emanuele Marchetti[1]

[1]Department of Earth Sciences, University of Firenze, Firenze, Italy, [2]Swiss Federal Institute for Forest, Snow and Landscape Research (WSL), Zurich, Switzerland

Key Points:

- Infrasound by debris-flows is generated by turbulence induced waves at the surface of the flow, mostly generated at channel steps or bends
- Infrasound peak frequency by debris-flows decreases with increasing flow magnitude, while seismic peak frequency is constant for all events
- Infrasonic and seismic energy radiation by debris-flows are strongly influenced by flow discharge and flow depth

Correspondence to:
G. Belli,
g.belli@unifi.it

Citation:
Belli, G., Walter, F., McArdell, B., Gheri, D., & Marchetti, E. (2022). Infrasonic and seismic analysis of debris-flow events at Illgraben (Switzerland): Relating signal features to flow parameters and to the seismo-acoustic source mechanism. *Journal of Geophysical Research: Earth Surface*, *127*, e2021JF006576. https://doi.org/10.1029/2021JF006576

Received 3 JAN 2022
Accepted 2 JUN 2022

Abstract Debris flows are among the most dangerous phenomena in mountain environment. Recently the use of seismic and infrasonic recordings has proven to be a powerful tool for studying and monitoring debris flows. However, open questions remain about how signal characteristics refllect flow parameters and fluid dynamic processes. We present a seismo-acoustic analysis of the debris flow activity between 2017 and 2019 at the Illgraben catchment (Switzerland). Seismic and infrasonic amplitudes (maximum root mean square amplitude [RMSA]) and peak frequencies are compared with flow measurements (front velocity, maximum flow depth and density). Front velocity, maximum depth, peak discharge and peak mass flux show a positive correlation with both infrasonic and seismic maximum RMSA, suggesting that seismo-acoustic amplitudes are influenced by these flow parameters. Comparison between seismo-acoustic peak frequencies and flow parameters reveals that, unlike seismic signals, characterized by a constant peak frequency regardless of the magnitude of the flow, infrasound peak frequency decreases with increasing flow velocity, depth and discharge. Our results suggest that infrasound and seismic waves are generated by different source processes, acting at the flow free surface and at the channel bed respectively. We propose that infrasound is likely generated by waves and oscillations that develop at the surface of the flow, which, according to fluid dynamics, are mostly generated wherever the flow encounters significant channel irregularities. Furthermore, the observed positive correlations between seismo-acoustic signal features and flow parameters highlight the potential to use infrasound and seismic measurements for debris-flow monitoring and risk management.

Plain Language Summary Debris flows represent a serious hazard in mountain environments and significant efforts are undertaken to develop automatic warning systems. We analyzed infrasonic (low-frequency sound) and seismic (ground vibrations) signals generated by the debris-flow activity at the Illgraben (Switzerland) between 2017 and 2019. Seismic and infrasonic signal features are compared with flow parameters. Positive correlations emerge between flow parameters and the amplitude of infrasonic and seismic signals, suggesting that the seismic and infrasonic radiation by debris flows is influenced by flow depth and discharge. Moreover, our results indicate that seismic and infrasonic waves are generated by different sources acting at the channel bed and at the flow surface respectively. For the seismic signal, presented results agree with previous models, which attribute the radiation of seismic waves to solid particle collisions, friction and fluid dynamic structures. Our novel observations allow to improve our understanding of the infrasound source within debris flows, being consistent with waves that develop at the surface of the flow depending on flow properties and channel irregularities. Finally, experimental results highlight how infrasound and seismic measurements could be successfully used to quantify remotely the magnitude of debris flows, thus opening new perspective for monitoring and risk management.

1. Introduction: Debris Flows

Debris flows are episodic gravitational currents of high density (~2,000 kg/m^3 (Wang et al., 2018)), consisting of highly concentrated mixtures of water, mud and solid debris particles in varying proportions (Coussot & Meunier, 1996). Their flow behavior has been described as intermediate between floods and landslides (e.g., Iverson & Vallance, 2001). Within debris flows, the solid fraction typically ranges between 50% and 90% (Coussot & Meunier, 1996), with solid particle sizes varying from clay to meter-sized boulders (Pérez, 2001).

Occurring on steep slopes of loose debris, debris flows are often initiated by water supply (Badoux et al., 2009), typically via intense rainfalls, natural or artificial dams collapses or rapid snowmelt (Dowling & Santi, 2014;

Takahashi, 1981). Debris flows tend to occur as several surges (Iverson, 1997) that flow long distances in steep torrential channels, with volumes commonly exceeding thousands of m^3 (Coussot & Meunier, 1996; Iverson, 1997). Typical debris-flow velocities range between 0.5 and 10 m/s (Johnson, 1970; Pierson, 1980; Sharp & Nobles, 1953), although velocities up to 20 m/s have been reported (Khegai et al., 1992).

Based on flow dynamics and solid fraction, a debris flow can be subdivided in three main flow parts: the boulder-rich front, the flow body and the flow tail (Costa & Williams, 1984; Coussot & Meunier, 1996; Iverson, 1997). The boulder-rich front transports rocks of all sizes and mud and acts as a granular flow with high solid fraction (50%–90%) (Iverson, 1997). It resists the overall gravity-driven motion as the flow body pushes it from behind (Iverson, 1997; Johnson & Rodine, 1984). The flow body is a debris laden flow with high solid fraction (50%–90%) but richer in mud than in boulders and is therefore more fluid and flows with lower basal friction than the front. The flow tail typically consists of a two-phase hyperconcentrated flow, with a lower solid fraction (40%–55%) (Pierson, 1985) and is characterized by a significant relative velocity between water-solid suspension and coarser solid particles (Coussot & Meunier, 1995; Smart & Jäggi, 1983), which, due to a reduced flow transport capacity, begin to settle (Coussot & Piau, 1994).

The destructive potential of debris flows, resulting from their high impact forces and their long runout distances, combined with their relative unpredictability, renders debris flows among the most dangerous natural hazards in mountain environments (Badoux et al., 2009). In addition, due to climate change and to an increased population pressure in mountain areas, the impact of debris flows on human lives and activities has increased in the last decades (Dowling & Santi, 2014). Nevertheless, the moderate flow velocities (typically <10 m/s) and the long runout distance make early warning possible if debris flows are detected rapidly upon their formation (Arattano & Marchi, 2005; Badoux et al., 2009).

Due to the complexity of the phenomenon and to the wide variability of flow types, geomorphologic features of the catchment and socio-economic settings of the affected areas, debris-flow monitoring is based on a wide range of approaches (see Arattano & Marchi (2005) and Hürlimann et al. (2019), for a review), involving rainfall forecast, catchment observations and in-channel measurements (Badoux et al., 2009). Recently, the use of seismic and infrasonic signals for the study and monitoring of debris flows has received scientific attention (Arattano, 1999; Burtin et al., 2009, 2014; Kogelnig et al., 2014; Lai et al., 2018; Marchetti et al., 2019; Walter et al., 2017). As a matter of fact, debris flows radiate elastic energy both into the ground and into the atmosphere, in the form of seismic waves and infrasound, respectively (Marchetti et al., 2019). These signals typically have emergent, cigar-shaped envelopes and show a wide variability in duration and amplitude.

Similarly to what has been observed for seismic energy radiation by rivers, attributed to solid particles collisions primed by bed load transport and to fluid dynamics effects (Burtin et al., 2008, 2009; Gimbert et al., 2014; Schmandt et al., 2013; Tsai et al., 2012), both theoretical and experimental studies suggest that within a debris-flow seismic waves are mostly generated by solid particle-bed collisions (Farin et al., 2019; Kean et al., 2015; Lai et al., 2018; Zhang, Walter, McArdell, Wenner, et al., 2021). These impacts produce fluctuations of the basal force exerted by the flow on the bed radiating high frequency seismic waves. In particular, particle collisions with the bed occur both in the form of single particle random impacts and in the form of force chains, which are networks of interacting particles that amplify the collision forces to the bed (Estep & Dufek, 2012; Zhang, Walter, McArdell, Wenner, et al., 2021). Although seismic energy is radiated along the entire debris flow, the boulder-rich debris-flow front appears to dominate seismic signal generation (Farin et al., 2019; Piantini et al., 2021; Zhang, Walter, McArdell, Wenner, et al., 2021). This was confirmed also in the field by Coviello et al. (2019), who analyzed the seismic energy produced by debris flows in the Gadria stream catchment (Eastern Italian Alps) showing that most energy transfer occurs during the passage of the surge fronts and is controlled by the mass and the velocity of each surge. Peak frequencies of debris-flow seismic signals depend only on source-to-receiver distance (Lai et al., 2018; Wenner et al., 2019), with peak frequencies decreasing with increasing distances from the flow front, due to stronger attenuation of higher seismic frequencies (Tsai et al., 2012).

Infrasound is generated whenever the atmosphere is perturbed by a rapid movement and propagates in the form of elastic longitudinal air waves. Marchetti et al. (2019) analyzed the infrasonic signals generated by three debris flows at the Illgraben (Switzerland), also performing an array analysis. They were able to reconstruct the signal modeling the generated infrasound as an incoherent superposition of signals resulting from multiple, simultaneously active infrasonic sources along the entire flow. In agreement with experimental observations on rivers,

infrasound radiation by debris flows is strongly affected by fixed locations along the channel, whenever the flow travels across dams or topography changes (Belli et al., 2021; Feng et al., 2014; Kudo, 1993; Marchetti et al., 2019). Specifically, in steep mountain channels infrasound is likely produced at dams as shooting water hits the stream bed downstream and triggers surface waves and splashes induced by turbulence that develops at the base of the free overfall (Tokyay & Yildiz, 2007). Feng at al. (2014), according to previous models based on large objects impacting water (Ostrovsky & Bedard, 2002), modeled infrasound waves generated at dams as the result of surface waves induced by water entering an absorption pool. In particular, they suggest a mechanism where water fall at dams generates local elevations of the water surface surrounded by rings of descending water levels which radiate infrasound as a dipole source (Feng et al., 2014). Therefore, debris flows, similarly to rivers, are expected to have multiple sources of infrasound, depending on flow dynamics and channel geometry (Marchetti et al., 2019). In addition, peak frequency of infrasound signals produced by debris flows is typically concentrated below 40 Hz (Chou et al., 2013) and seems to scale with flow volumes (Marchetti et al., 2019).

Seismo-acoustic networks have proven to be powerful tools for the study and monitoring of mass movements, such as pyroclastic density currents, snow avalanches (Allstadt et al., 2018; Ripepe et al., 2009; Ulivieri et al., 2011; Yamasato, 1997) and debris flows (Kogelnig et al., 2014; Lai et al., 2018; Marchetti et al., 2019; Schimmel & Hübl, 2016). Concerning debris flows, most efforts focused on the early detection of the events (Arattano, 1999; Chmiel et al., 2021; Kogelnig et al., 2011; Lai et al., 2018; Liu et al., 2015; Schimmel & Hübl, 2016; Walter et al., 2017). For seismic waves, several theoretical source mechanisms have been proposed (Farin et al., 2019; Kean et al., 2015; Lai et al., 2018; Zhang, Walter, McArdell, de Haas, et al., 2021), mostly based on the model developed by Tsai et al. (2012) for seismic noise by rivers. However, in our knowledge, clear on field validation of proposed seismic model are still missing and no accurate source models have been proposed yet for infrasound by debris flows. As a result, it is not yet fully understood how flow parameters and processes affect resulting seismo-acoustic signal features.

Along the lines of the work by Marchetti et al. (2019), in this study, we present a seismo-acoustic analysis of debris-flow activity in the Illgraben catchment (Switzerland) during summers 2017–2019. The main features, such as maximum amplitude and peak frequency, of infrasonic and seismic signals are compared with flow measurements in order to investigate how flow features influence the seismo-acoustic energy radiation by debris flows and if the two wavefields are generated by the same fluid dynamic or physical processes.

2. Study Site and Monitoring System

The Illgraben catchment, situated in Switzerland's Canton Valais, (Figure 1), is one of the most active debris-flow basins in the Alps (Badoux et al., 2009) and among the best instrumented sites worldwide. The catchment has an area of ∼10 km^2 (Schlunegger et al., 2009) and an elevation that ranges from the 2,716 m (Above Mean Sea Level [AMSL]) of the Illhorn mount to the 850 m (AMSL) of the debris fan apex. The upper basin (∼5 km^2) is drained by the steep Illgraben torrent that, after a ∼5 km path (∼3 km in the active upper catchment, until the fan apex and ∼2 km along the fan axis) flows into the Rhone River at an elevation of 610 m (AMSL). The Illgraben channel has an average slope of 9° (16%) in the upper basin, that decreases to 5.7°(10%) downstream of the fan apex (Badoux et al., 2009). The erosion of the stream along the upper Illgraben catchment frequently produces rockfalls and landslides along the steep (>40°) catchment slopes (Schlunegger et al., 2009) and provides sediment supply for Illgraben's debris-flow events (Bennet et al., 2013; Berger et al., 2011). The debris-flow activity has led, in the last 16–17 ky (Ivy-Ochs et al., 2008; Schurch et al., 2016), to the formation of the large ∼500 million of m^3 debris fan, on the southern side of the Rhone valley (Schlunegger et al., 2009), which nowadays is densely inhabited.

Debris flows occurring in the Illgraben catchment are characterized by a considerable variability in size, duration and in the hydraulic, physical and compositional features (Badoux et al., 2009). Typical events are granular debris flows with high solid fraction (50%–90%) and transporting blocks up to several meters in diameter, mostly concentrated in the flow front (Coussot & Meunier, 1996). Other flow types occur as well, ranging from muddy debris flows, to hyperconcentrated flows, to flood flows, and despite having a lower solid fraction, they may all transport boulders with a mean diameter as large as the flow depth (Badoux et al., 2009). Moreover, many of the flows occur as flash floods, with the flow depth rising from zero to several meters in a short time span (few seconds or minutes), with strong implications for flow impact and associated hazard.

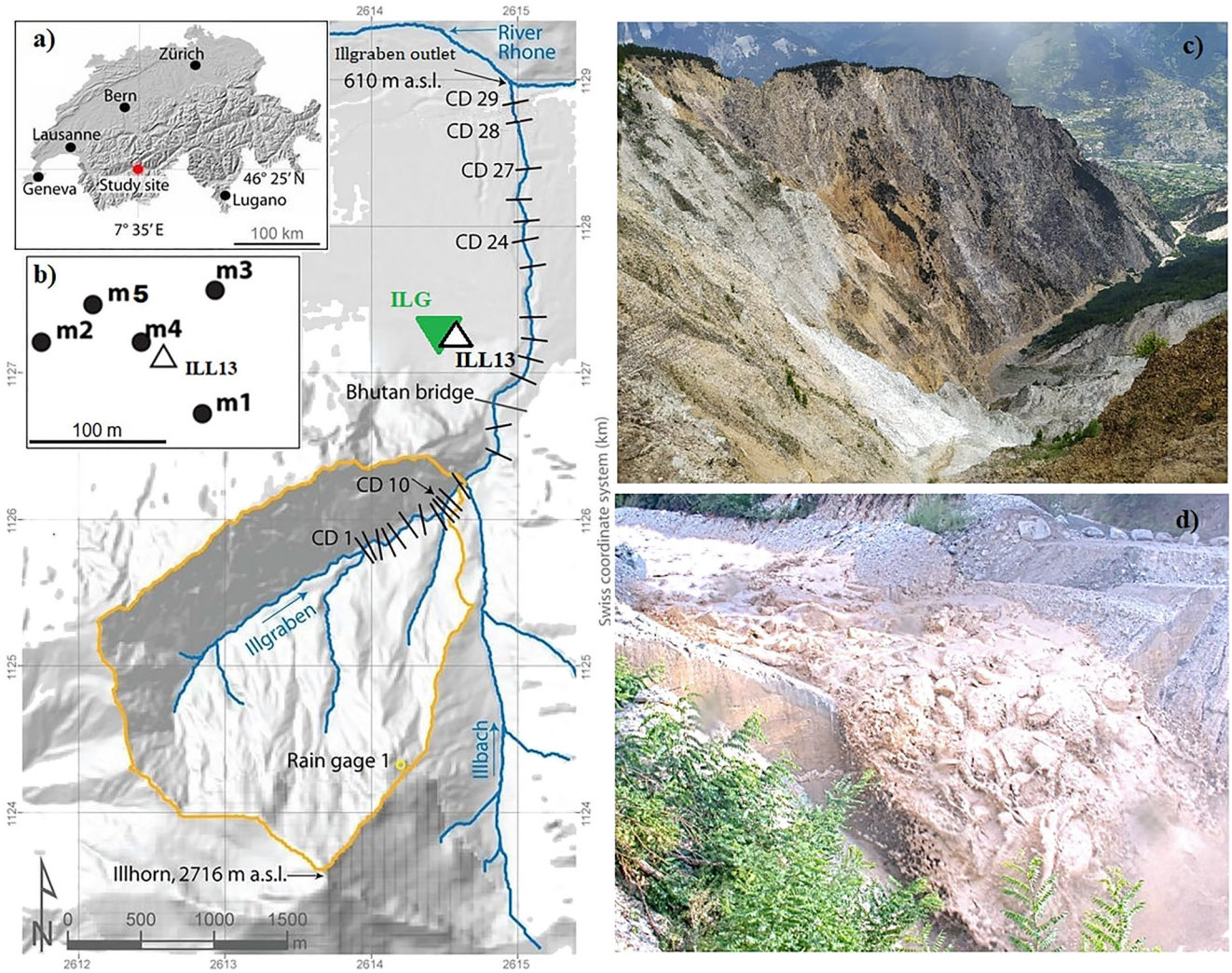

Figure 1. Left: Map of the geographic setting of the Illgraben catchment, showing the extension of the upper catchment (yellow line), the position of ILG infrasound array (green triangle) and of the ILL013 seismometer (white triangle) used in this study. The black bars with alpha-numerical labels indicate the position of Illgraben check dams (CD). (a) Position of the Illgraben in Switzerland. (b) Relative geometry of the ILG infrasound array and seismic sensor. (c) Picture of the Illgraben catchment taken from its south-west rim (source: Giacomo Belli); (d) photograph of an Illgraben debris flow shooting over CD29 (event on 2019/08/11; source: WSL).

At Illgraben, debris flows generally occur between May and October (Badoux et al., 2009; Berger et al., 2011). Such a clear seasonal activity results from common triggering processes, like the summer rain storms (Hürlimann et al., 2003; McArdell et al., 2007), or snowmelt (Wenner et al., 2019). Debris-flow initiation is also possible in the absence of precipitation, or as a result of rapid snow melt or when natural dams of lakes formed by landslides sudden fail, giving rise to a sufficient runoff for the triggering of debris flows (Costa & Schuster, 1988; Evans & Clague, 1994).

In order to mitigate the impact and risk associated with Illgraben debris-flow activity and to minimize erosion on the torrent channel (Henderson, 1996; Tokyay & Yildiz, 2007), a series of check dams (CDs) were constructed along the channel (Figure 1). This led to a substantial reduction of the debris-flows damage potential; indeed, most debris flows no longer overtop the channel bank and significant damage last occurred in 1961 when a road bridge was destroyed (Badoux et al., 2009).

Since 2000, the Swiss Federal Institute for Forest, Snow and Landscape Research (WSL) installed a scientific observatory devoted to debris-flow monitoring (Hürlimann et al., 2003; McArdell et al., 2007; Rickenmann et al., 2001), consisting of flow stage sensors (laser, radar (Arattano & Marchi, 2005)), geophones installed on check dams for front-velocity estimation and video cameras (Hürlimann et al., 2003), as well as a large force plate

which has been used to determine bulk flow properties such as the mass density and force-fluctuations (McArdell et al., 2007; Schlunegger et al., 2009). The separate debris-flow alert system, which is under the responsibility of the local municipality, combines catchment status observations, related to general sediment availability and the possible presence of torrent-blocking landslides, and direct in-channel flow threshold detection measurements. This system has recently been modified, but for the data presented herein it consisted of radar flow-depth measurements and geophone sensors for determining flow velocity (Badoux et al., 2009) and the force plate for density. In both the WSL scientific observatory and the operational warning system, debris-flow front arrival times are detected with geophones installed on the concrete of CDs 1, 27, and 29 (Figure 1) (Walter et al., 2017), and differences in arrival times are used to calculate the flow velocity. Recently, debris-flow activity at Illgraben has also been monitored by a dense seismic network (e.g., Chmiel et al., 2021; Walter et al., 2017; Wenner et al., 2019) and by a small aperture infrasound array (Marchetti et al., 2019).

3. Instrumental Set-Up

For this study we used infrasound and seismic data recorded on the fan apex, at a distance of ∼600 m from the fan apex, and hydraulic data collected by in-torrent measurements. Infrasound data are recorded by array ILG (Figure 1), that has been installed during the debris-flow season (late spring and summer) since 2017 (Marchetti et al., 2019). ILG is a FIBRA array (www.item-geophysics.it), designed to operate with fiber optic connection of up to 5 array elements. Here, sensors are arranged in a triangular geometry (Figure 1) and an aperture (maximum distance between two array elements) of 160 m, optimized to analyze infrasound signals in the 1–10 Hz frequency band. Each array element is equipped with a differential pressure transducer with a sensitivity of 400 mV/Pa in the pressure range of ±12.5 Pa and a flat frequency response between 0.01 and 200 Hz. Analogue pressure data are sampled at each array element at 50 Hz and digitized at 16 bits. The installation site is a flat forested area to minimize wind noise.

Seismic data have been collected by a Lennarzt LE3D 1s triaxial seismometer with an eigenfrequency of 1 Hz. In this work we used data from a seismic station that is collocated with the infrasonic array (ILL13, Figure 1), that is part of the dense seismic network deployed during the debris-flow season since 2016 (Wenner et al., 2019). The seismometer, deployed near the central element of the infrasonic array, is placed into a plastic bag buried in a 30 cm deep pit, subsequently backfilled with soil. Ground motion is recorded with a Nanometrics Centaur digitizer. Data are collected at 100 Hz and continuously telemetered to the Swiss Seismological Service.

Debris-flow hydraulic and physical data are collected by in-torrent measurements, provided by sensors closely located along the stream path or directly within the channel, as described above. In particular we used flow-depth measurements at CD29, flow velocities calculated from differences in arrival times at CD27 or CD28 and CD29, and flow density values estimated from force plate measurements that are performed at CD29 (Figure 1).

4. Data

4.1. The Event Database

In the period 2017–2019, 18 debris flows were observed at Illgraben (Table 1). Events are characterized by a high variability in size and in the hydraulic features (Table 1, Figure 2). For the events in 2017 and 2018, the force plate was not operational as a result to damage during a major flow event in 2016 and the flow depth measurements and related volume calculations are less accurate than after the re-installation of the force plate in 2019. Total volumes are estimated by integrating flow discharge over the entire debris flow wave (Schlunegger et al., 2009); obtained values vary between few thousands of m^3 and 10^5 m^3 and reveal that the majority of Illgraben debris flows are small ($V < 20{,}000$ m^3), although several large flows ($V > 80{,}000$ m^3) are commonly observed (Figure 2a).

Estimated flow front velocity (v), calculated as the ratio between along-channel distance and the differences in the flow front arrival times between CD27 (or CD28) and CD29, range from <1 m/s to >8 m/s, suggesting a wide variability in flow dynamics, probably reflecting differences in composition and water content. Typical events have front velocities between 6.5 and 7.5 m/s (∼36% of the events with measured velocity), but events with low velocity ($v < 2$ m/s) are observed too (Figure 2b). Flow velocity varies significantly along the channel, depending both on flow size and runout and on channel geometry (slope) (Schürch et al., 2011). In addition, uncertainties on flow velocity measurement arise from detecting the flow front arrival times, which is often challenging,

Table 1
Timing and Hydraulic and Physical Features of the Illgraben 2017–2019 Debris Flows

Date	CD1 arrival time (UT)	Volume (m^3)	Front velocity (m/s) (CD27-28-29)	Maximum flow depth (m) (CD29)	Bulk density (Kg/m^3)	Froude number	Unit peak flow discharge (m^2/s)	Unit peak mass flux (t/m•s)
2017/05/29	16:58:31	100,000	6.7	2.8	n.m.	1.3	18.76	n.c.
2017/06/03	23:27:38	9,000	5.1	1.9	n.m.	1.2	9.69	n.c.
2017/06/14	19:30:48	35,000	7.2	2.0	n.m.	1.6	14.40	n.c.
2018/06/11	10:46:39	n.m.	n.m.	n.m.	n.m.	n.c.	n.c.	n.c.
2018/06/12	18:29:16	n.m.	n. m.	n.m.	n.m.	n.c.	n.c.	n.c.
2018/07/25	16:56:40	n.m.	4.7	1.2	n.m.	1.4	5.64	n.c.
2018/08/08	17:49:25	n.m.	6.7	n.m.	n.m.	n.c.	n.c.	n.c.
2019/06/10	17:02:51	1,800	0.9	0.77	1,887	0.3	0.69	1.31
2019/06/10	22:01:17	5,200	2.5	0.42	1,631	1.2	1.05	1.71
2019/06/20	09:12:17	n.m.	n.m.	n.m.	n.m.	n.c.	n.c.	n.c.
2019/06/21	19:34:42	97,000	6.6	2.59	1,870	1.3	17.09	31.97
2019/07/01	23:00:29	73,000	3.9	1.61	1,971	1.0	6.28	12.38
2019/07/02	22:09:28	4,100	0.8	0.77	2333	0.3	0.62	1.44
2019/07/03	16:43:15	n.m.	n.m.	n.m.	n.m.	n.c.	n.c.	n.c.
2019/07/15	03:40:21	9,900	3.4	0.54	2191	1.5	1.84	4.02
2019/07/26	17:33:12	110,000	8.7	1.05	2223	2.7	9.14	2.03
2019/08/11	17:02:34	88,000	7.0	1.80	2323	1.7	12.60	2.93
2019/08/20	16:40:59	6,100	0.9	0.44	2031	0.4	0.40	0.80

Note. The force plate was not present in 2017–2018, consequently some parameters are reported as n.m. (not measured) and some derived quantities as n.c. (not computed). Froude number, unit peak flow discharge, and unit peak mass flux are computed using Equation 2, Equation 3, and Equation 4, respectively.

especially for smaller flows. We therefore estimate the velocity over a 140–480 m long reach of the channel to get a more time-averaged estimate of front velocity.

Maximum flow depth (H), ranging from ~0.6 to 2.8 m, is measured at CD 29 (Walter et al., 2017; Wenner et al., 2019). The maximum flow depth in debris flows is generally recorded when the flow front passes under the flow altimeters and therefore corresponds to the front height (Pierson, 2020), but the recorded value can be affected by the presence of flow waves. Out of the 13 debris flows for which a flow depth measurement is available, a water level ≥2 m was recorded only for 3 events (Figures 2c and Table 1). Comparison between front velocity and maximum flow depth revealed that the flow velocity appears to be at least partially controlled by the flow depth, with higher flow velocity generally corresponding to larger flow depth (Figure 2d), in agreement with theory of open channel flows predicting higher velocity for larger-depth flows (Henderson, 1996). The red line in Figure 2d represents the critical velocity (v_c) and therefore marks the distinction between subcritical ($v < v_c$) and supercritical flows ($v > v_c$) (Henderson, 1996). Critical velocity is equal to the velocity ($v_w = v_c$) with which a wave or perturbation resulting from any disturbance or obstacles in open channel flow propagates over the water surface and is defined as (Henderson, 1996):

$$v_c = \sqrt{gH} \tag{1}$$

where g is the acceleration of gravity. Criticality is the state at which the specific energy of the flow is minimum (Henderson, 1996) and the flow velocity (v) equals the critical velocity ($v = v_c = v_w$). Flow conditions relative to criticality are described by the Froude number (Fr), that is for rectangular channels, which is a good assumption for the Illgraben, is defined as (Henderson, 1996):

$$Fr = \frac{v}{\sqrt{Hg}} \tag{2}$$

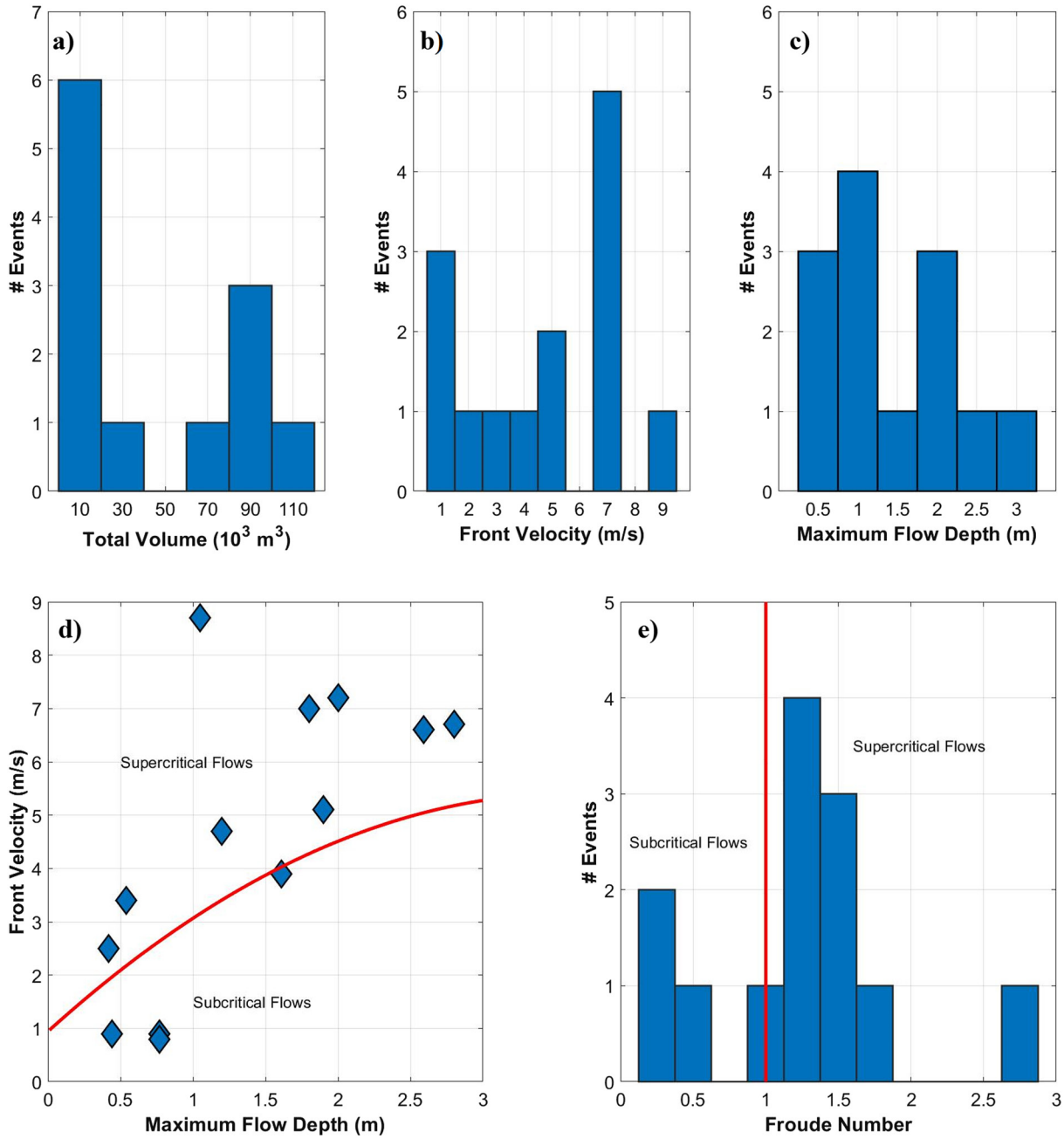

Figure 2. Histograms showing the distribution of total volume (a), front velocity (b), maximum flow depth (c) and Froude number (d) among the 2017–2019 Illgraben debris-flow events. In (d) the vertical red line marks the boundary between subcritical flows ($Fr < 1$) and supercritical flows ($Fr > 1$).

The Froude number expresses the ratio between flow velocity (v) and the velocity (v_w) surface perturbations (Henderson, 1996). Computed Froude numbers (Figures 2e and Table 1), together with the comparison between debris-flow front velocity and critical velocity (Figure 2d), reveals that almost all Illgraben debris flows fall into the supercritical domain ($Fr > 1$), indicating that the flow is faster than surface perturbations, which therefore are able to propagate only downstream (Henderson, 1996). In particular, we observe that among analyzed events, all debris flows with $H > 1$ m are supercritical (Figure 2d), except for the 2019/07/01 event, which falls in the critical domain ($Fr = 1$). Uncertainties resulting from the measurements of flow depth and flow velocities combine in the computation of the Froude number. In particular, for larger flows with roll waves, where the surface flow waves are about 1/3 to 1/2 of the maximum measured depth, it is not clear which value of flow depth to use to calculate

the Froude number. However, our values, computed using maximum flow depth values and front velocities, are still representative of the flow front conditions.

Flow bulk density (ρ) is computed as the mass/volume ratio at the force plate deployed on the brink of CD29, measuring the flow weight and the depth of the flow over the force plate and considering the plate area and channel geometry (McArdell, 2016; McArdell et al., 2007). Obtained values, available for nine events, vary between 1,600 and 2,400 kg/m^3 (Table 1), reflecting differences in solid fraction and water content.

Again, assuming a rectangular channel section, reasonable for the Illgraben, in order to further investigate the relationship between hydraulic parameters and seismo-acoustic signals, we combine front velocity, maximum flow depth and flow density values to derive the peak flow discharge per unit channel width (Q_u) and the peak mass flux per unit channel width (MF_u) as:

$$Q_u = H \cdot v \tag{3}$$

$$MF_u = Q_u \cdot \rho \tag{4}$$

Obtained values are listed in Table 1. If we assume that the width of the Illgraben channel between CD28 and CD29, where velocity and depth measurements are collected, remains constant over time, thereafter the computed peak discharge and peak mass flux per unit channel width reflect the peak volumetric discharge and mass flux, respectively. The stable width channel assumption is reasonable considering that the Illgraben channel is stabilized by the constructions of the check dams.

4.2. The Seismic and Infrasonic Database

Our seismo-acoustic data set consists of seismic and infrasonic data of the 18 debris-flow events (Figure 3a), recorded by the ILG infrasonic array and the ILL13 seismometer (Figure 1). Infrasound data for the 2018/08/08 event are missing. In particular, for this study we used data recorded at m1 sensor (Figure 1), expect for the 2018/07/25 event, for which we used data recorded at m5, because m1 sensor was not working at the time of the event.

Events are recorded as long lasting (30–100 min), emergent, cigar shaped infrasonic and seismic signals. Peak-to-peak seismic amplitudes span 2 orders of magnitude, ranging from ∼3 μm/s, observed for the 2018/06/11 and 2018/06/12 events, up to ∼200 μm/s, observed for the 2017/05/29 seismogram. In the infrasound record, peak-to-peak amplitudes vary from a maximum of ∼1.5 Pa, observed for the 2017/05/29 debris flow (2 orders of magnitude above the back-ground noise of around 0.05 Pa) down to 0.2 Pa observed for the 2019/07/15 event. The six smallest events did not produce discernible signal above noise levels (Figure 3a). The high-amplitude infrasound transients observed for several events, and clearly visible in Figure 3a, are infrasonic signals generated by lightning activity and thus not related to debris flows (Marchetti et al., 2019). The effect of the lighting activity on infrasound signal is particularly evident for the 2019/07/02 and 2019/07/26 debris flows, for which the infrasound signal produced by the rainstorm, having comparable amplitudes as the debris-flow infrasonic signal, strongly affects the entire waveform (Figure 3a).

In general, seismic signals appear to be clearer, that is, characterized by a higher signal-to-noise ratio, compared to infrasonic ones. Indeed, whereas every reported debris-flow event generated a distinguishable seismic signal, at least 6 smaller magnitude debris flows did not generate a distinguishable infrasound signal above the back-ground noise level (Figure 3a). Therefore, the present analysis of Illgraben debris flows has been limited to 11 out of 18 events in case of infrasound, while it has been carried out on all 18 events in case of seismic signals (Table 2).

5. Data Analysis and Results

5.1. RMSA and Spectral Analysis of Seismo-Acoustic Signals

The root mean square amplitude (RMSA) was calculated on 1–20 Hz band-pass filtered infrasound and seismic signals, over 1-min-long moving time windows along the entire duration of the events (Figure 3b). The signal envelope, obtained from the RMSA analysis, shows a marked asymmetry resulting from an amplitude rising time that is generally shorter than the amplitude fall-off tail. Maximum RMSA varies between 0.035 and 0.208 Pa for infrasound and between 0.43 and 27.8 μm/s for seismic signals (Table 2). The small range of

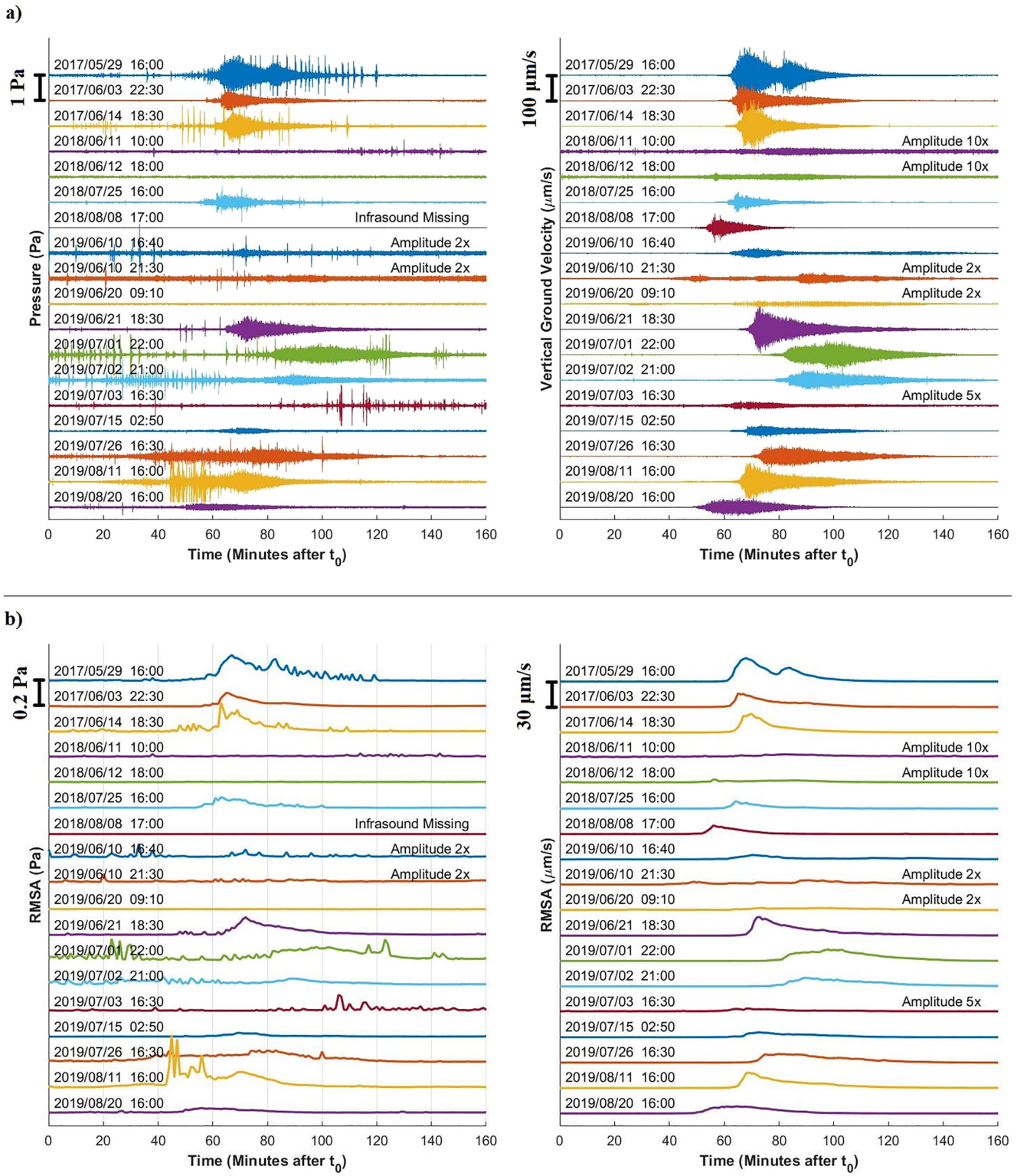

Figure 3. (a) Infrasound (left) and seismic (right) waveforms of the 18 debris flow at Illgraben between 2017 and 2019. (b) Infrasound (left) and seismic (right) Root Mean Square Amplitude (RMSA) envelopes computed over one-minute-long moving time windows for all 18 events. For all signals, timing is expressed in minutes after the time reported on the left of each trace.

Table 2
Peak Time, Maximum RMSA and Peak Frequency (f_P) of Infrasound and Seismic Signals

Debris flow events	Infrasound RMSA peak time (UT)	Max infrasound RMSA (Pa)	Infrasound peak frequency (Hz) (f_P)	Seismic RMSA peak time (UT)	Max seismic RMSA (μm/s)	Seismic peak frequency (Hz) (f_P)
2017/05/29	17:07	0.208	3.4	17:08	27.80	6.9
2017/06/03	23:35	0.113	5.8	23:35	16.12	7.2
2017/06/14	19:39	0.166	4.8	19:40	22.13	7.3
2018/06/11	n. d.	n. d.	n. d.	11:22	0.46	n. d.
2018/06/12	n. d.	n. d.	n. d.	18:56	0.43	n. d.
2018/07/25	17:03	0.090	n. c.	17:04	8.52	7.2
2018/08/08	no infrasound	no infrasound	no infrasound	17:56	10.12	7.3
2019/06/10	n. d.	n. d.	n. d.	17:50	5.38	7.3
2019/06/10	n. d.	n. d.	n. d.	23:01	2.78	7.3
2019/06/20	n. d.	n. d.	n. d.	09:37	0.50	7.5
2019/06/21	19:42	0.145	4.6	19:43	22.04	7.1
2019/07/01	23:38	0.112	4.8	23:38	13.78	6.9
2019/07/02	22:29	0.064	not used (*)	22:30	10.31	7.3
2019/07/03	n. d.	n. d.	n. d.	17:39	0.81	n. d.
2019/07/15	03:59	0.035	6.0	04:03	6.01	7.3
2019/07/26	17:47	0.098	not used (*)	17:50	10.39	7.1
2019/08/11	17:11	0.128	4.7	17:09	18.32	7.0
2019/08/20	16:56	0.044	6.0	17:05	8.45	7.3

Note. Peak frequencies were computed using Equation 5. "n.d." and "n.c." stand for "not detectable" and "not computable," respectively. The symbol (*) marks the events for which infrasound peak frequency is strongly affected by rainstorms that occurred during the peak phase of the flow and produced infrasonic noise approximately of the same magnitude as the debris-flow signal.

variation of maximum infrasound RMSA, compared to the seismic RMSA, results from the infrasonic analysis having been performed only on the 11 events for which a clear infrasound signal was recorded; the 6 lower magnitude debris-flow events were excluded.

Seismic and infrasound waveforms were also analyzed in the frequency domain by computing the Power Spectral Density (PSD) (Figures 4a and 4b). The seismic signals of the events of 2018/06/11, 2018/06/12, and 2019/07/03 are characterized by a very low signal-to-noise ratio, therefore the PSD was not computed for these three events. Due to the recording sensor malfunction, for the event of 2018/07/25 the infrasonic PSD is not computable. Therefore, the infrasound generated by this event was excluded from the frequency analysis below. PSD curves of seismic and infrasound signals are shown in Figure 4. Infrasound and seismic signals are marked by significantly different peak frequencies. Infrasound is characterized by a broad (1–10 Hz) frequency content, whose peak changes from event to event (Figure 4a). In contrast, the seismic spectrum is characterized by a stable broad peak around 7 Hz for all events. The peak decreases rapidly below 2–3 Hz, well above the eigenfrequency of the Lennartz 3D seismometer, and above 20 Hz, well below the Nyquist frequency (50 Hz) of the A/D converter.

Figures 4c and 4d show the comparison between maximum spectral amplitude (max PSD) and peak frequency values (f_P) of the signals. These were computed from PSDs as the weighted average of the frequency (f) over the spectral amplitude (Sa) (Table 2). For each event, the weighted average was calculated around ($df = 2$ Hz) of the manually picked peak frequency value (f_{mp}) as:

$$f_P = \frac{\sum_i Sa_i f_i}{\sum_i Sa_i} \forall f_i \in \left[f_{mp} - df, f_{mp} + df\right] \quad (5)$$

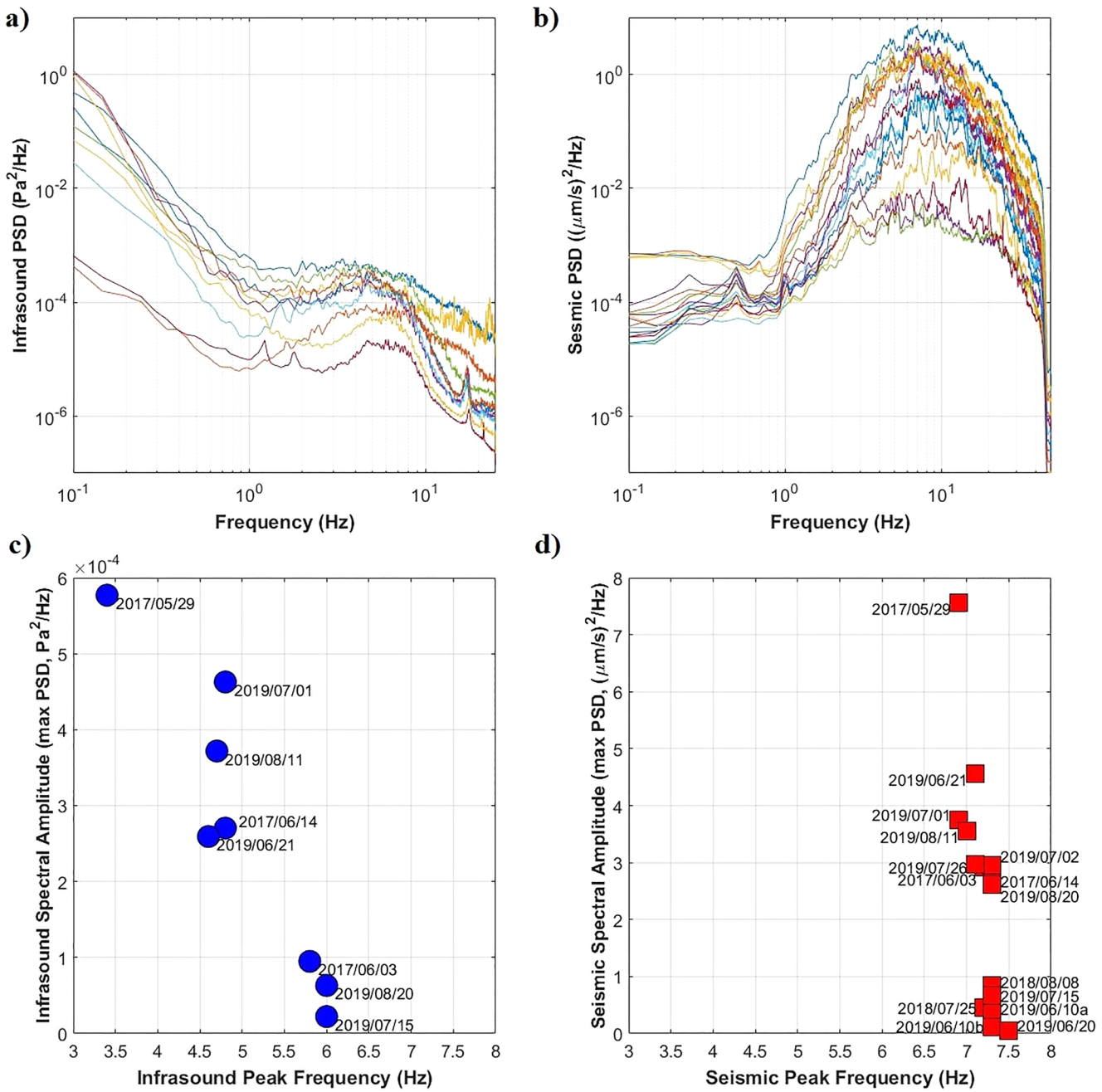

Figure 4. Power spectral density of infrasound (a) and seismic (b) records of the Illgraben debris-flow events. Spectral peak amplitudes of infrasonic (c) and seismic (d) signals as a function of peak frequencies. In (d) the two events on 2019/06/10 are marked in chronological order with the letters "a" and "b".

f_{mp} is appropriately picked as a frequency value roughly corresponding to the location of the peak of the signal spectrum; its role is just to set the center of the frequency interval over which the exact peak frequency (f_P) is computed with Equation 5: The large width of the interval (4 Hz in our case) makes the initial choice of f_{mp} irrelevant at first approximation.

Obtained infrasonic peak frequencies vary between 3.4 and 6 Hz (Table 2, Figure 4c), while seismic peak frequency is stable for all events, with values ranging between 6.8 and 7.2 Hz (Table 2, Figure 4d).

The frequency content of the infrasound generated by the events on 2019/07/02 and 2019/07/26 is strongly affected by the simultaneous thunderstorms (Figure 3a). Therefore, the infrasonic signals generated by these two events are excluded from Figure 4c and from the frequency analysis shown below in Figure 6.

In general, infrasound peak frequency tends to decrease with increasing spectral peak amplitude (Figure 4c). In contrast, such a relation between peak frequency and maximum spectral amplitude is much weaker or absent for seismic signals (Figure 4d).

5.2. Relationship Between Seismo-Acoustic Amplitudes and Hydraulic Data

In order to investigate how flow parameters and what fluid dynamic processes influence the seismo-acoustic energy radiation by debris flows, the peak RMSA values (Table 2) of infrasound and seismic data are compared with available hydraulic data (Figure 5). The comparison is limited to events for which both seismo-acoustic and hydraulic data are available. Results show a positive correlation between amplitude of seismo-acoustic signals (infrasonic and seismic max RMSA) and flow parameters.

Concerning front velocity (Figures 5a and 5b), RMSA appears to increase with velocity, with the exemption of the slowest (1 m/s) and fastest (9 m/s) events, that prevents defining a clear correlation function.

A clearer linear relationship, expressed with the Pearson correlation factor (R), is obtained considering the maximum flow depth (Figure 5c, 5d, $R = 0.943$ and $R = 0.952$ for infrasound and seismic signals respectively), and the peak discharge per unit channel width (Figure 5e, 5f, $R = 0.943$ and $R = 0.936$ for infrasound and for seismic signals, respectively). In particular the lowest amplitude signals are recorded for the smallest flows, with flow depth as low as 1 m and unit discharge as low as 3 m^2/s, while signal amplitude increases with the flow depth and/or discharge.

Compared with seismo-acoustic maximum RMSA (Figures 5g and 5h), also the unit peak mass flux shows a linear relation ($R = 0.920$ for infrasound, $R = 0.885$ for seismic), suggesting that events with larger mass flux produce larger amplitude infrasound and seismic signals. However, in the comparison between seismo-acoustic amplitudes and unit mass flux, the combination of uncertainties linked to discharge and density estimations for the six selected events (1,930–2,240 kg/m^3, Table 1) and the lower number of available observations has to be considered when evaluating the quality of the obtained relation.

5.3. Relation Between Seismo-Acoustic Peak Frequencies and Hydraulic Data

In order to investigate if the spectral content of infrasonic and seismic signals generated by debris flows is correlation a specific hydraulic parameter or physical process within the flow, available hydraulic data were compared to infrasonic and seismic signal peak frequencies (Figure 6), determined from computed PSD curves (Figure 4, Table 2). A systematic difference between peak frequencies of seismic and infrasound signals is observed (Figure 6): Seismic peak frequency is stable around 7.1 Hz for all events (7.1 ± 0.2 Hz) regardless of the size of the event, flow depth, velocity or discharge. On the contrary, infrasound peak frequency changes from event to event and decreases form 6–3.4 Hz with increasing front velocity (Figure 6a), maximum flow depth (Figure 6b) or discharge per channel width (Figure 6c). Whereas the number of observations is still limited, this inverse relation between peak infrasound frequency and flow parameters seems however to be limited to larger events, exceeding velocities of 4 m/s, flow depth of 1–1.5 m and peak discharge for unit width of 10 m^2/s, while the relation is less evident for smaller and slower events.

6. Discussion

The results presented in this study highlight general trends between infrasound and seismic observations of debris-flow activity at Illgraben and an evident positive correlation between maximum RMSA and flow parameters. Both seismic and infrasound energy radiation appears to be strongly influenced by the flow characteristics, as suggested by the linear relations between maximum RSMA and flow properties (Figure 5): Higher flow velocities and/or larger flow depths generally produce higher amplitude infrasonic and seismic debris-flow signals. Flow velocity and flow depth are measured ~1,500 m further downstream from the position of minimum distance between the channel and the recording seismo-acoustic sensors. This introduces some uncertainties

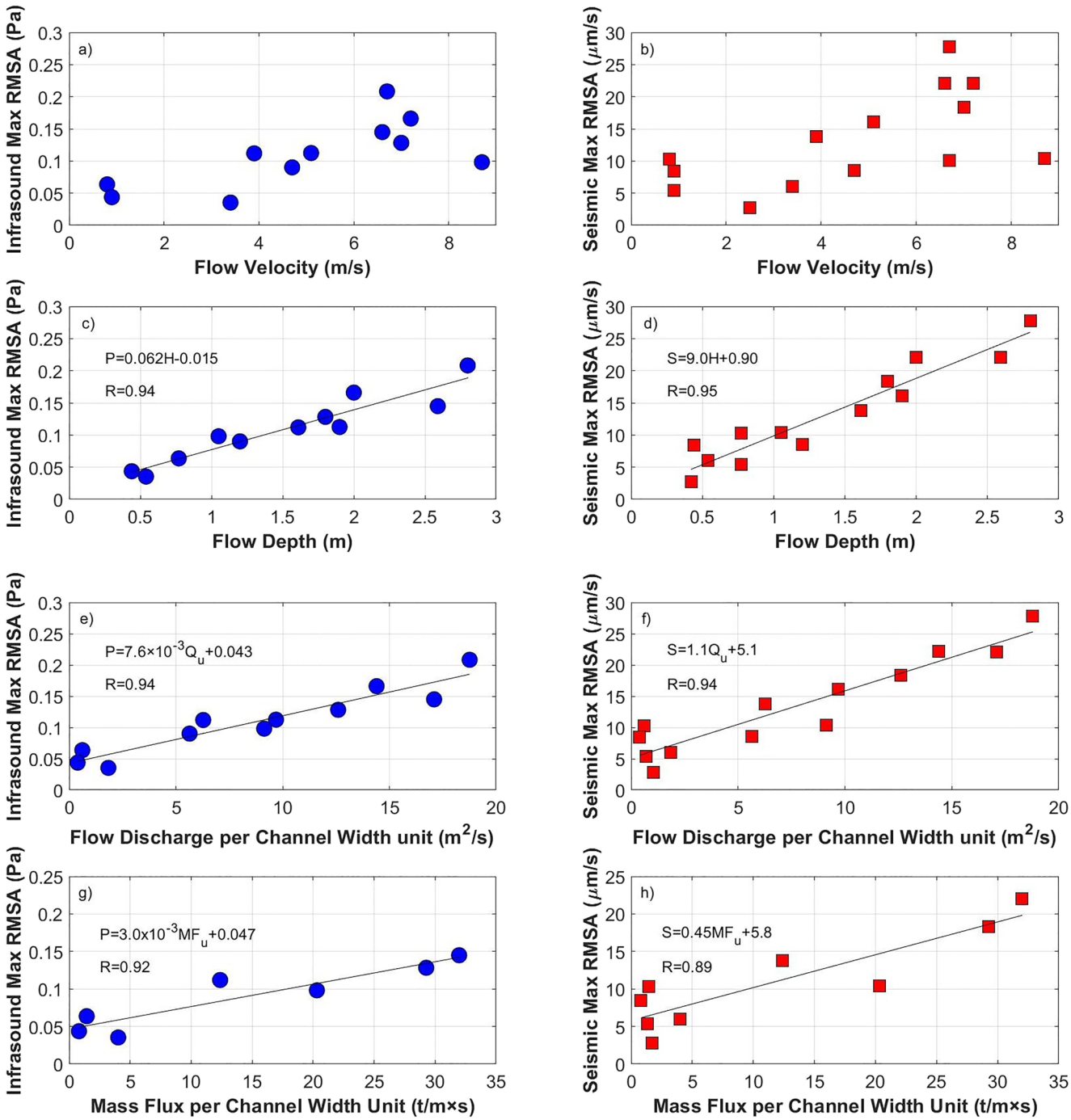

Figure 5. Relations between maximum RMSA of infrasonic (left side, blue circles) and seismic (right side, red squares) debris-flow signals and flow velocities (a and b), maximum flow depth (c and d), flow peak discharge per unit channel width (e and f) and peak mass flux per unit channel width (g and h). In each diagram the best fit regression line is plotted and its equation is specified within the diagram. In the equations, P (in Pa) stands for infrasound max RMSA, S (in μm/s) for seismic max RMSA, H is the flow depth (in m), Q_u is the flow peak discharge per unit channel width (in m^2/s) and MF_u is the peak mass flux per unit channel width (in t/m•s). For each best fit regression line, we computed the Pearson correlation factor R.

when comparing seismo-acoustic signals with flow parameters, since the measured values could differ from the actual value the flow had in the sector closest to the recording sensors, which is expected to generate higher amplitude component of the recorded seismo-acoustic signals. However, a relative comparison is still permissible. In addition, the seismic and infrasonic source is an extended and complex one, where the front, the body

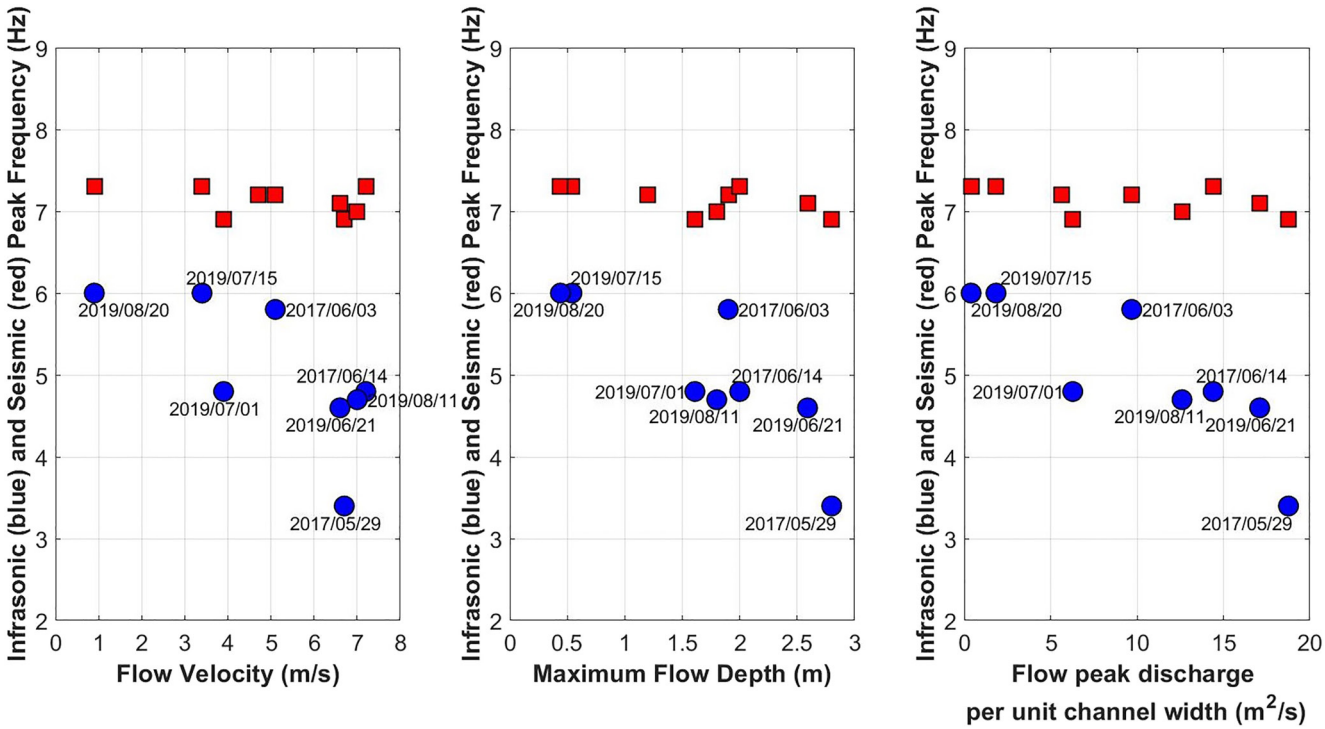

Figure 6. Relations between peak frequency of infrasonic (blue circles) and seismic (red squares) signals, generated by Illgraben debris flows, and front velocity (a), maximum flow depth (b) and peak flow discharge per unit channel width (c). In each diagram, data points reflect debris-flow events for which the corresponding parameters (seismo-acoustic peak frequencies and front velocity, flow depth or discharge) are available or computable.

and the tail all act simultaneously but creating signal of different amplitude depending on the flow characteristics (Farin et al., 2019; Marchetti et al., 2019). Therefore, the analysis of the seismic-acoustic radiation would require locating the radiating source. However, many studies have shown that the flow front dominates the generated seismic signal (Coviello et al., 2019; Zhang, Walter, McArdell, de Haas et al., 2021; Zhang, Walter, McArdell, Wenner, et al., 2021), while for infrasound Marchetti et al. (2019) found that the maximum signal amplitude is generated when the barycentre of the extended source representing the flow is located at the minimum distance to the infrasonic sensor. Therefore, we believe that our comparison between the seismic and infrasonic signal as a whole and the hydraulic data is permissible, since the velocity is actually the front velocity, and the maximum depth is measured in correspondence of the flow front (Pierson, 2020).

Despite some uncertainty for single data points, the measured high values of the Pearson correlation factor (R) shown in Figures 5c and 5d and in Figures 5e and 5f, suggest that flow depth and peak discharge per unit channel width control the amplitude of recorded seismo-acoustic signals. For a complete characterization of the debris-flow seismicity, a compared analysis with the boulder size would be required too, because grain size has shown to be dominant controlling factor in impact generated seismic waves (Tsai et al., 2012). Nevertheless, this will involve further data analysis of videos of the flow to determine the boulder size that could be addressed in future studies.

The observed positive linear relationship between seismic amplitude and flow discharge is in perfect agreement with Andrade et al. (2022), who also found a linear relation between flow discharge and seismic peak amplitude radiated by lahars observed at Tungurahua and Cotopaxi volcanoes. Our results are also consistent with findings by Coviello et al. (2019) who, analyzing debris-flow events in Gadria catchment (Italy), found that generated seismic amplitudes correlate positively with the kinetic energy of the flow. Despite these similarities the infrasound and seismic signals show a decoupled frequency content. The seismic peak frequency is almost constant (6.9–7.3 Hz), regardless of the magnitude of the event (Figure 6). The measured value of ~7 Hz is in good agreement with the minimum distance of ≈550 m of the seismometer to the Illgraben torrent, in accordance with the model proposed by Tsai et al. (2012) for seismic noise produced by bed load transport, that explains

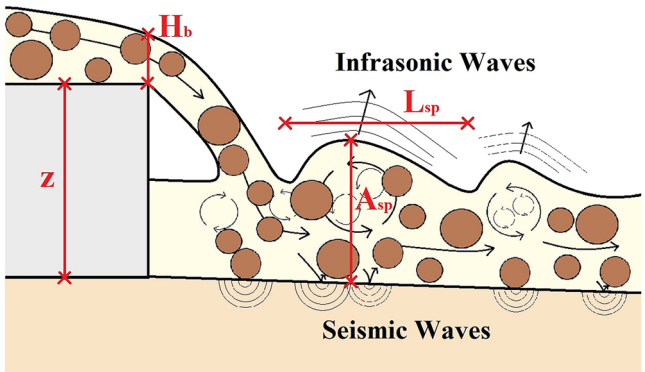

Figure 7. Sketch of the conceptual model proposed in this work for infrasonic and seismic waves radiation by debris flows. The sketch was designed developing the scheme by Tokyay and Yildiz (2007), which describes the dimensions of waves developing at the base of a supercritical free overfall, and adapting it for seismo-acoustic radiation mechanisms by debris-flows. z is the height of the topographic step; H_b is the flow depth over the brink of the free overfall; L_{sp} and A_{sp} are respectively the length and the amplitude (measured from the ground) of the waves or water splashes generated downstream the fall.

the frequency content in terms of propagation effects of surface waves and that was observed to be valid also for debris flows (Lai et al., 2018) and also specifically for the Illgraben site (Wenner et al., 2019).

As opposed to the seismic data, infrasound peak frequency varies between 3.4 and 6 Hz and appears to systematically decrease with increasing maximum spectral amplitude (Figure 4c). This suggests that the more energetic the infrasound source within debris flows, the lower the peak frequency. In addition, it is observed that infrasound peak frequency decreases also with increasing event magnitude (flow depth and/or discharge) (Figure 6), suggesting that larger flows (events with larger discharge and/or flow depth) radiate lower frequency infrasound. This result is consistent with the findings by Marchetti et al. (2019), who analyzed only 3 debris-flow events that occurred in 2017 at the Illgraben (also included in this work), and by Coco et al. (2021), who modeled a decrease in peak frequency of infrasonic waves radiated by water flow downstream a topographic step (dam) with increasing flow depth or the height of the step.

The inverse trend observed between infrasound peak frequency and flow magnitude holds for all considered hydraulic parameters (v, H and Q_u), but the best fit is obtained with the flow depth and with the flow peak discharge per unit channel width (Figures 6b and 6c). The best inverse relation is observed for larger events ($H > 1.5$ m, $Q_u > 10$ m^2/s). For smaller events, infrasound peak frequency seems to be almost independent of flow discharge. This could be at least partly explained by the signal-to-noise ratio, which affects determination of the peak frequency of smaller events. Small events imply a source of small amplitude and high frequency, of the same order as the ambient noise.

Such a variation of the infrasound frequency content suggests a complex relation to flow properties. According to fluid dynamic models and flume experiments on water flows, irregularities (waves and splashes) are induced at the flow surface by turbulence structures generated in the flow for water falling at free overfalls (Coco et al., 2021; Feng et al., 2014; Tokyay & Yildiz, 2007), such as check-dams, or for flow interaction with the channel roughness (Horoshenkov et al., 2013). In particular, Tokyay and Yildiz (2007), performing flume experiments on supercritical water flows, observed that at the base of a supercritical ($Fr > 1$) free overfall, there is strong energy dissipation (up to >50% of the initial energy) and the development of heavy water splashes at the flow's free surface (Figure 7), due to the flow impacting the floor and setting up vigorous circulation and turbulence. They observed that the height of the water splashes or waves (A_{sp}) linearly scales with the Froude number (Fr) (which increases with flow velocity) and with the square root of the product between the flow depth over the brink of the fall (H_b) and the height of the fall (z) as (Tokyay & Yildiz, 2007):

$$A_{sp} = 0.4532\, F_r \sqrt{z\, H_b} \tag{6}$$

where A_{sp} is measured from the channel bottom (Figure 7). Such a flow behavior is to be expected also in case of debris flows that undergo free overfall at the check-dams, since computation of the Froude number (Figure 2e) revealed that almost all larger ($H > 1$ m) Illgraben debris flows fall into the supercritical conditions. This scenario, predicting increased turbulence downstream dams, is in general agreement with Feng et al. (2014) who, based on the model by Ostrovsky and Bedard (2002) on infrasound produced by the fall of large objects into water, proposed that infrasonic waves are preferentially radiated at the base of dams by a dipole-type source generated by water falling into the absorption pole.

We did not account for elastic wave propagation. Relative signal comparison is still permissible, because the dominant signals are related to the passage of the "loudest" flow sections past the point along the torrent which is closest to the recording station. For the seismic signals, our observed correlations thus agree with investigations using different Illgraben seismometers, which did quantify modifications of seismic frequency content and amplitudes as a result of propagation: The amplitude of high-frequency (>1 Hz) seismic signals of Illgraben events was found to scale with the effective particle size in the coarse-grained flow front (Zhang, Walter,

McArdell, deHaas, et al., 2021 and with flow depth (Zhang, Walter, McArdell, Wenner, et al., 2021). This agrees with theoretical predictions by Farin et al. (2019), although the exact scaling is difficult to capture, given that the flow parameters like flow depths, flow velocity, grain size distribution, particle sorting and water content all influence seismogenesis as well as each other.

Based on all presented results (Figures 5 and 6), previous theoretical (Farin et al., 2019; Gimbert et al., 2014; Tsai et al., 2012) and numerical models (Coco et al., 2021), as well as field observations of infrasound and seismic signals radiated by debris flows (Belli et al., 2021; Kean et al., 2015; Lai et al., 2018; Marchetti et al., 2019), we propose a simplified conceptual source mechanism for seismo-acoustic waves radiated by debris flows (Figure 7).

Concerning the seismic wavefield, because of the limited constraints we provide in this study, we rely on existing models for seismic energy radiation by rivers (Burtin et al., 2008; Schmandt et al., 2013; Tsai et al., 2012) and debris flows (Huang et al., 2007; Burtin et al., 2009; Kean et al., 2015; Lai et al., 2018; Zhang, Walter, McArdell, de Haas, et al., 2021), which attribute the generation of seismic waves to solid particle collisions and friction with the channel bed and banks and fluid dynamic structures. In accordance with all these studies, our results suggest that the radiation of seismic waves by debris flows is influenced by flow discharge (Figure 5), that in turn controls the solid transport capability of the flow. An increased flow discharge leads to an increased transport capability of the solid fraction, with debris flows able to transport boulders with a diameter as large as the flow depth (Badoux et al., 2009), a wider development of fluid dynamic structures (Tokyay & Yildiz, 2007) and a larger wetted perimeter. Despite the different contribution cannot be evaluated with our seismic data only and further dedicated field analysis and study we be required, it is reasonable to expect that this scenario results in stronger and more frequent solid particle impacts and in an increased friction with channel bed and banks and thus leads to larger stress fluctuations at the base of the flow, thus radiating higher amplitude seismic signal. In contrast, it does not affect the frequency content, that, being controlled solely by the source-to-receiver distance (Tsai et al., 2012), is expected to remain stable, in agreement with the experimental relations observed here (Figures 5 and 6). Experimental confirmations would involve the comparison with boulder size data from video analysis, that needs to be addressed in future studies.

However, our findings clearly demonstrate decoupled sources for seismic waves and infrasound, separately acting at the ground or at the surface of the flow respectively. Indeed, the lack of infrasound energy observed for smaller events suggests that the infrasonic source mechanism develops effectively only above a certain discharge rate, while seismic energy radiation is observed regardless of the flow size. This evidence also allows us to infer that debris flows are likely more effective as seismic sources than as infrasound sources, especially for smaller magnitude events.

In addition, for all events we observe that the seismic peak frequency is systematically higher than the infrasonic one. This is not imputable to seismic propagation effects, which involve stronger attenuation of the higher frequencies for seismic waves while they do not affect the frequency of infrasound over such short propagation distances, and therefore demonstrates an originally different frequency content for the two wavefields, that in turn reflect separated seismo-acoustic sources.

The suggested decoupled sources are also in agreement with previous seismo-acoustic observations of debris flows. Differently from seismic signals, that appear to be dominated by the flow front (Farin et al., 2019; Piantini et al., 2021; Zhang, Walter, McArdell, de Haas, et al., 2021), the infrasound by debris-flow is mostly generated in fixed position downstream significative channel irregularities (Belli et al., 2021; Marchetti et al., 2019), regardless of the position of the flow front.

The results presented in this study, particularly the inverse relation of infrasound frequency to flow properties, also suggest additional constraints on the source mechanism of infrasound by debris flows. Infrasound by debris flows is produced as the moving flow surface perturbates the atmosphere generating pressure disturbances in the air. In agreement with infrasound array analysis of debris flows at the Illgraben (Belli et al., 2021; Marchetti et al., 2019), we propose that infrasound by debris-flows is radiated by turbulence induced free surface waves and oscillations. These infrasonic sources are likely active along the entire length of the flow, but, for the case of the Illgraben, are enhanced downstream of check dams. Indeed, in agreement with fluid dynamic predictions, these non-stationary water surface displacements are mostly generated where the turbulence is stronger and more powerful and, therefore, wherever the flow encounters significant channel irregularities (Feng et al., 2014;

Henderson, 1996; Tokyay & Yildiz, 2007). Therefore, these channel irregularities, such as topographic steps (check dams) and steep bends in the planform geometry of the channel, result as preferential source of infrasound.

This interpretation is consistent with the experimental relations observed between infrasound maximum amplitude and debris-flow characteristics (Figure 5). An increase in the flow depth or discharge enhances the development of a higher and more intense fluid dynamic turbulence in the flow. This induces larger waves and water splashes at the flow free surface (Tokyay & Yildiz, 2007), that in turn cause stronger pressure perturbations in the atmosphere and hence higher-amplitude infrasound waves (Ostrovsky & Bedard, 2002).

The proposed infrasound source mechanism based on turbulence induced non-stationary surface oscillations, developing mostly at topography changes (e.g., free overfall at drop/dams) or other channel irregularities (e.g., bends), is also in agreement with the observed decrease of the peak frequency with the increase of the depth and discharge (Figure 6). Larger flows generate surface oscillations with larger wavelengths (L_{sp}) (Tokyay & Yildiz, 2007), which, for the same flow speed, result in longer periods of the infrasonic sources and therefore radiate lower frequency infrasound. This agrees with numerical modeling (Coco et al., 2021) of infrasound waves produced by a water flow, reporting a decrease of infrasound frequency when discharge increases for a fixed dam height, while it predicts the absence of significant infrasound radiation, regardless of the flow discharge, when the flow occurs within flat channels lacking any irregularities (bed roughness topographic steps, bends). Furthermore, the infrasound source mechanism based on turbulence-induced surface oscillations discussed here also qualitatively explains the observed wide infrasound spectrum: turbulence structures, like eddies, cover a wide range of dimensions over which they also generate non-stationary flow surface displacements. This produces a wide frequency spectrum of pressure variation in the atmosphere (Feng et al., 2014).

Finally, the experimental relationships shown in this study suggest how infrasonic and seismic data might be used for monitoring purposes at the Illgraben and could provide, in real-time and without in-torrent measurement, an indirect estimate of flow depth and/or discharge from seismo-acoustic observations. Both the amplitude (Figure 5) and, for larger events, the frequency (Figure 6) of recorded infrasound could be used to estimate the discharge of the flow remotely. This further highlights the potential to use seismo-acoustic signals for debris-flow monitoring and risk management, not only for event detection (Chmiel et al., 2021; Kogelnig et al., 2014; Marchetti et al., 2019; Walter et al., 2017), but also for real time estimates of debris-flow depth and or discharge.

7. Conclusions

We present an analysis of the infrasonic and seismic signals generated by debris-flow activity in the Illgraben catchment (Switzerland) during the period 2017–2019. In order to investigate how flow parameters and what flow processes influence the seismo-acoustic energy radiation by debris flows, the amplitude and the spectral content of infrasonic and seismic signals are compared with flow measurements, that is, flow front velocity, maximum flow depth and bulk flow density.

Results show that infrasonic and seismic maximum RMSA positively correlate with front velocity and scale linearly with maximum depth and flow peak discharge per unit channel width, computed as the product of front velocity and maximum depth. This suggests that flow velocity and flow depth combine to strongly influence the radiation of both seismic and infrasonic waves by debris flows. The resulting positive linear relationship between seismic amplitude and flow discharge is in excellent agreement with Andrade et al. (2022) and Coviello et al. (2019), who, analyzing lahars and debris flows respectively, also observed positive relation between seismic amplitudes and flow discharge or kinetic energy of the flow.

Spectral analysis of seismo-acoustic signals reveals that infrasonic and seismic signals of debris flows are characterized by different peak frequencies. We show that unlike seismic signals that, in agreement with previous studies (Tsai et al., 2012; Wenner et al., 2019), are characterized by a nearly constant peak frequency regardless of the flow size, infrasound peak frequency decreases with increasing front velocity, flow depth and discharge.

Based on presented results and taking into account previous models and experiments, we propose a decoupled source mechanism for seismic and infrasound radiation by the flow, with the two wavefields being generated by different processes acting at the ground and at the flow surface respectively. Results agree with previous models and observation of seismic energy radiation by rivers (Burtin et al., 2008; Schmandt et al., 2013; Tsai et al., 2012) and debris flows (Burtin et al., 2009; Kean et al., 2015; Lai et al., 2018; Zhang, Walter, McArdell, de Haas,

et al., 2021), indicating that seismic waves are generated by solid particle collisions and friction with the riverbed and banks and by fluid dynamic structures.

For infrasound we propose a source mechanism in which infrasonic waves are generated by turbulence-induced waves and oscillations that develop at the free surface of the flow (Feng et al., 2014; Marchetti et al., 2019; Ostrovsky & Bedard, 2002). The formation of such surface waves is enhanced wherever the flow encounters channel irregularities, such as significative topographic steps and steep bends (Belli et al., 2021; Coco et al., 2021; Tokyay & Yildiz, 2007). Here, we propose that an increase in the flow discharge enhances the development of larger turbulent flow structures, that generate larger waves and turbulence-induced water splashes at the flow free surface (Tokyay & Yildiz, 2007), thus radiating higher-amplitude and lower frequency infrasound waves (Coco et al., 2021; Marchetti et al., 2019). Numerical (Coco et al., 2021) and experimental (Tokyay & Yildiz, 2007) studies suggest that the flow discharge and the dimensions of irregularities affect the wavelength of turbulence-induced surface structures thus controlling the frequencies of recorded infrasound.

Presented results, linking seismo-acoustic signal features to flow properties, allow to add constraints to the source processes of the two wavefields within debris flows and thus provide a valuable observational basis for future theoretical and experimental studies. Moreover, the observed relationships between seismo-acoustic signal features and flow parameters suggests how infrasound and seismic signals could be used for the near real-time estimation of the size of an ongoing debris flow, at locations where seismo-acoustic recordings of past events are available, highlighting their potential for debris-flow monitoring and risk management.

Data Availability Statement

Infrasound data recorded by ILG arrays, and debris-flow parameters provided by WSL (Swiss Federal Institute for Forest, Snow and Landscape Research), used to achieve all the findings and create all the figures in this paper, are freely available in the Open Science framework repository (https://osf.io/36nvq/) (Belli et al., 2022a, 2022b, 2022c). Seismic data from the Illgraben network are collected under the network code XP (https://doi.org/10.12686/sed/networks/xp) and all seismic data will be openly available after a 2-year embargo (in 2023) via the archives in the Swiss Seismological Service, http://www.seismo.ethz.ch/en/research-and-teaching/products-software/waveform-data/ (Belli et al., 2022a, 2022b, 2022c), and in the European Integrated Data Archive (EIDA), http://www.orfeus-eu.org/data/eida/ (Belli et al., 2022a, 2022b, 2022c).

Acknowledgments
The authors are grateful to reviewers Kate Allstadt, Emma Surinach, and Velio Coviello and Elizabeth Silber for their helpful comments and suggestions; they gave us in the revision phase of the manuscript. Open Access Funding provided by Universita degli Studi di Firenze within the CRUI-CARE Agreement.

References

Allstadt, K. E., Matoza, R. S., Lockhart, A. B., Moran, S. C., Caplan-Auerbach, J., Haney, M. M., et al. (2018). Seismic and acoustic signatures of surficial mass movements at volcanoes. *Journal of Volcanology and Geothermal Research*, *364*, 76–106. https://doi.org/10.1016/j.jvolgeores.2018.09.007

Andrade, S. D., Almeida, S., Saltos, E., Pacheco, D., Hernandez, S., & Acero, W. (2022). A simple and general methodology to calibrate seismic instruments for debris flow quantification: Application to Cotopaxi and Tungurahua volcanoes (Ecuador). *Landslides*, 1–13.

Arattano, M. (1999). On the use of seismic detectors as monitoring and warning systems for debris flows. *Natural Hazards*, *20*(2–3), 197–213.

Arattano, M., & Marchi, L. (2005). Measurements of debris flow velocity through cross-correlation of instrumentation data. *Natural Hazards and Earth System Sciences*, *5*(1), 137–142.

Badoux, A., Graf, C., Rhyner, J., Kuntner, R., & McArdell, B. W. (2009). A debris flow alarm system for the alpine Illgraben catchment: Design and performance. *Natural Hazards*, *49*(3), 517–539.

Belli, G., Marchetti, E., Walter, F., McArdell, B., Chmiel, M., & Wenner, M. (2021). Investigating infrasound sources within Illgraben debris flows. *EGU General Assembly*. online, 19–30 Apr 2021, EGU21-1226. https://doi.org/10.5194/egusphere-egu21-1226

Belli, G., Walter, F., McArdell, B., Gheri, D., & Marchetti, E. (2022a). Illgraben debris-flow seismic data from the Illgraben network. [Dataset]. European Integrated Data Archive (EIDA). Retrieved from http://www.orfeus-eu.org/data/eida/

Belli, G., Walter, F., McArdell, B., Gheri, D., & Marchetti, E. (2022b). Infrasonic recordings and flow parameters of the 2017–2019 Illgraben debris-flow events. [Dataset]. Open Science framework OSF. Retrieved from https://osf.io/36nvq/

Belli, G., Walter, F., McArdell, B., Gheri, D., & Marchetti, E. (2022c). Illgraben debris-flow seismic data from the Illgraben network. [Dataset]. Swiss Seismological Service. Retrieved from http://www.seismo.ethz.ch/en/research-and-teaching/products-software/waveform-data/

Bennett, G. L., Molnar, P., McArdell, B. W., Schlunegger, F., & Burlando, P. (2013). Patterns and controls of sediment production, transfer and yield in the Illgraben. *Geomorphology*, *188*, 68–82. https://doi.org/10.1016/j.geomorph.2012.11.029

Berger, C., McArdell, B. W., & Schlunegger, F. (2011). Direct measurement of channel erosion by debris flows, Illgraben, Switzerland. *Journal of Geophysical Research*, *116*(F1), F01002. https://doi.org/10.1029/2010jf001722

Burtin, A., Bollinger, L., Cattin, R., Vergne, J., & Nábělek, J. L. (2009). Spatiotemporal sequence of Himalayan debris flow from analysis of high-frequency seismic noise. *Journal of Geophysical Research*, *114*(F4), F04009. https://doi.org/10.1029/2008jf001198

Burtin, A., Bollinger, L., Vergne, J., Cattin, R., & Nábělek, J. L. (2008). Spectral analysis of seismic noise induced by rivers: A new tool to monitor spatiotemporal changes in stream hydrodynamics. *Journal of Geophysical Research*, *113*(B5), B05301. https://doi.org/10.1029/2007jb005034

Burtin, A., Hovius, N., McArdell, B. W., Turowski, J. M., & Vergne, J. (2014). Seismic constraints on dynamic links between geomorphic processes and routing of sediment in a steep mountain catchment. *Earth Surface Dynamics*, *2*(1), 21. https://doi.org/10.5194/esurf-2-21-2014

Chmiel, M., Walter, F., Wenner, M., Zhang, Z., McArdell, B. W., & Hibert, C. (2021). Machine Learning improves debris flow warning. *Geophysical Research Letters*, *48*(3), e2020GL090874. https://doi.org/10.1029/2020gl090874

Chou, H. T., Chang, Y. L., & Zhang, S. C. (2013). Acoustic signals and geophone response of rainfall-induced debris flows. *Journal of the Chinese Institute of Engineers*, *36*(3), 335–347.

Coco, M., Marchetti, E., & Morandi, O. (2021). Numerical modeling of infrasound energy radiation by debris flow events. *Pure and Applied Geophysics*, (6), 1–13. https://doi.org/10.1007/s00024-021-02759-2

Costa, J. E., & Schuster, R. L. (1988). The formation and failure of natural dams. *The Geological Society of America Bulletin*, *100*(7), 1054–1068.

Costa, J. E., & Williams, G. P. (1984). Debris-flow dynamics: US geological survey open file report 84-606. In *VHS videotape*.

Coussot, P., & Meunier, M. (1995). Experimental study of debris flows. *Journal of Hydraulic Engineering*, *121*(5), 438–440.

Coussot, P., & Meunier, M. (1996). Recognition, classification and mechanical description of debris flows. *Earth-Science Reviews*, *40*(3–4), 209–227.

Coussot, P., & Piau, J. M. (1994). Rheology of very concentrated suspensions of force-free particles. *Les Cahiers de Rhéologie*, *13*, 266–277.

Coviello, V., Arattano, M., Comiti, F., Macconi, P., & Marchi, L. (2019). Seismic characterization of debris flows: Insights into energy radiation and implications for warning. *Journal of Geophysical Research: Earth Surface*, *124*(6), 1440–1463.

Dowling, C. A., & Santi, P. M. (2014). Debris flows and their toll on human life: A global analysis of debris flow fatalities from 1950 to 2011. *Natural Hazards*, *71*(1), 203–227.

Estep, J., & Dufek, J. (2012). Substrate effects from force chain dynamics in dense granular flows. *Journal of Geophysical Research*, *117*(F1), F01028. https://doi.org/10.1029/2011jf002125

Evans, S. G., & Clague, J. J. (1994). Recent climatic change and catastrophic geomorphic processes in mountain environments. In *Geomorphology and natural hazards* (pp. 107–128). Elsevier.

Farin, M., Tsai, V. C., Lamb, M. P., & Allstadt, K. E. (2019). A physical model of the high-frequency seismic signal generated by debris flows. *Earth Surface Processes and Landforms*, *44*(13), 2529–2543.

Feng, H. N., Yang, Y. C., Chunchuzov, I. P., & Teng, P. X. (2014). Study on infrasound from a water dam. *Acta Acustica united with Acustica*, *100*(2), 226–234.

Gimbert, F., Tsai, V. C., & Lamb, M. P. (2014). A physical model for seismic noise generation by turbulent flow in rivers. *Journal of Geophysical Research: Earth Surface*, *119*(10), 2209–2238.

Henderson, F. M. (1996). Open channel flow.

Horoshenkov, K. V., Nichols, A., Tait, S. J., & Maximov, G. A. (2013). The pattern of surface waves in a shallow free surface flow. *Journal of Geophysical Research: Earth Surface*, *118*(3), 1864–1876. https://doi.org/10.1002/jgrf.20117

Huang, C. J., Yin, H. Y., Chen, C. Y., Yeh, C. H., & Wang, C. L. (2007). Ground vibrations produced by rock motions and debris flows. *Journal of Geophysical Research*, *112*(F2), F02014. https://doi.org/10.1029/2005jf000437

Hürlimann, M., Coviello, V., Bel, C., Guo, X., Berti, M., Graf, C., et al. (2019). Debris flow monitoring and warning: Review and examples. *Earth-Science Reviews*, *199*, 102981. https://doi.org/10.1016/j.earscirev.2019.102981

Hürlimann, M., Rickenmann, D., & Graf, C. (2003). Field and monitoring data of debris flow events in the Swiss Alps. *Canadian Geotechnical Journal*, *40*(1), 161–175.

Iverson, R. M. (1997). Hydraulic modeling of unsteady debris flow surges with solid-fluid interactions. In *Proceedings, first international conference on debris flow hazards mitigation: Mechanics, prediction, and assessment: Hydraulics division* (pp. 550–560). American Society of Civil Engineers.

Iverson, R. M., & Vallance, J. W. (2001). New views of granular mass flows. *Geology*, *29*(2), 115–118.

Ivy Ochs, S., Kerschner, H., Reuther, A., Preusser, F., Heine, K., Maisch, M., et al. (2008). Chronology of the last glacial cycle in the European Alps. *Journal of Quaternary Science: Published for the Quaternary Research Association*, *23*(6), 559–573.

Johnson, A. M. (1970). *Physical processes in geology: A method for interpretation of natural phenomena; intrusions in igneous rocks, fractures, and folds, flow of debris and ice*. Freeman.

Johnson, A. M., & Rodine, J. R. (1984). In D. Brunsden, & D. B. Prior (Eds.), *Debris flow (Chapter 8). Slope instability*.

Kean, J. W., Coe, J. A., Coviello, V., Smith, J. B., McCoy, S. W., & Arattano, M. (2015). Estimating rates of debris flow entrainment from ground vibrations. *Geophysical Research Letters*, *42*(15), 6365–6372.

Khegai, A. Y., Popov, N. V., Plekhanov, P. A., & Keremkulov, V. A. (1992). *Experiments at the Chemolgan Debris Flow Testing Ground, Kazakhstan, Landslide News* (Vol. 6, pp. 27–28). Jpn. Landslide Soc.

Kogelnig, A., Hübl, J., Suriñach, E., Vilajosana, I., & McArdell, B. W. (2014). Infrasound produced by debris flow: Propagation and frequency content evolution. *Natural Hazards*, *70*(3), 1713–1733.

Kogelnig, A., Hübl, J., Suriñach, E., Vilajosana, I., Zhang, S., Yun, N., & McArdell, B. (2011). A study of infrasonic signals of debris flow. In *Proceedings of 5th international conference on debris-flow hazards: Mitigation, mechanics, prediction and assessment* (pp. 563–572).

Kudo, N. (1993). Control of infrasonic noise from a waterfall. *Journal of Low Frequency Noise, Vibration and Active Control*, *12*(4), 149–155.

Lai, V. H., Tsai, V. C., Lamb, M. P., Ulizio, T. P., & Beer, A. R. (2018). The seismic signature of debris flows: Flow mechanics and early warning at Montecito, California. *Geophysical Research Letters*, *45*(11), 5528–5535.

Liu, D. L., Leng, X. P., Wei, F. Q., Zhang, S. J., & Hong, Y. (2015). Monitoring and recognition of debris flow infrasonic signals. *Journal of Mountain Science*, *12*(4), 797–815.

Marchetti, E., Walter, F., Barfucci, G., Genco, R., Wenner, M., Ripepe, M., et al. (2019). Infrasound array analysis of debris flow activity and implication for early warning. *Journal of Geophysical Research: Earth Surface*, *124*(2), 567–587.

McArdell, B. W. (2016). Field measurements of forces in debris flows at the Illgraben: Implications for channel-bed erosion. *International Journal of Erosion Control Engineering*, *9*(4), 194–198.

McArdell, B. W., Bartelt, P., & Kowalski, J. (2007). Field observations of basal forces and fluid pore pressure in a debris flow. *Geophysical Research Letters*, *340*(7). https://doi.org/10.1029/2006gl029183

Ostrovsky, L. A., & Bedard, A. J. (2002). (Vol. 2, pp. 873–875). On generation of infrasound by large objects falling into water. *IEEE International Geoscience and Remote Sensing Symposium*.

Pérez, F. L. (2001). Matrix granulometry of catastrophic debris flows (December 1999) in central coastal Venezuela. *Catena*, *45*(3), 163–183.

Piantini, M., Gimbert, F., Bellot, H., & Recking, A. (2021). Genesis and propagation of exogenous sediment pulses in mountain channels: Insights from flume experiments with seismic monitoring. *Earth Surface Dynamics Discussions*, 1–25.

Pierson, T. C. (1980). Erosion and deposition by debris flows at Mt Thomas, north Canterbury, New Zealand. *Earth Surface Processes*, *5*(3), 227–247.

Pierson, T. C. (1985). *Effects of slurry composition on debris flow dynamics, rudd canyon, Utah. Delineation of landslide, flash flood, and debris flow hazard in Utah*. Utah Water Research Laboratory, Utah State University, General series UWRL/G.

Pierson, T. C. (2020). *Flow behavior of channelized debris flows Mount St. Helens Washington. Hillslope processes* (pp. 269–296). Routledge.
Rickenmann, D., Hürlimann, M., Graf, C., Näf, D., & Weber, D. (2001). Murgang-beobachtungsstationen in der Schweiz. *Wasser, Energie, Luft*, *93*(1), 1–8.
Ripepe, M., De Angelis, S., Lacanna, G., Poggi, P., Williams, C., Marchetti, E., et al. (2009). Tracking pyroclastic flows at Soufrière Hills volcano. *Eos, Transactions American Geophysical Union*, *90*(27), 229–230.
Schimmel, A., & Hübl, J. (2016). Automatic detection of debris flows and debris floods based on a combination of infrasound and seismic signals. *Landslides*, *13*(5), 1181–1196.
Schlunegger, F., Badoux, A., McArdell, B. W., Gwerder, C., Schnydrig, D., Rieke-Zapp, D., & Molnar, P. (2009). Limits of sediment transfer in an alpine debris flow catchment, Illgraben, Switzerland. *Quaternary Science Reviews*, *28*(11–12), 1097–1105.
Schmandt, B., Aster, R. C., Scherler, D., Tsai, V. C., & Karlstrom, K. (2013). Multiple fluvial processes detected by riverside seismic and infrasound monitoring of a controlled flood in the Grand Canyon. *Geophysical Research Letters*, *40*(18), 4858–4863. https://doi.org/10.1002/grl.50953
Schürch, P., Densmore, A. L., Ivy-Ochs, S., Rosser, N. J., Kober, F., Schlunegger, F., et al. (2016). Quantitative reconstruction of late Holocene surface evolution on an alpine debris flow fan. *Geomorphology*, *275*, 46–57. https://doi.org/10.1016/j.geomorph.2016.09.020
Schürch, P., Densmore, A. L., Rosser, N. J., & McArdell, B. W. (2011). Dynamic controls on erosion and deposition on debris-flow fans. *Geology*, *39*(9), 827–830.
Sharp, R. P., & Nobles, L. H., (1953). Mudflow of 1941 at Wrightwood, southern California. *Geological Society of America Bulletin*, *64*(5), 547–560.
Smart, G., & Jäggi, M. (1983). Mitteilung. 64. Versuchsanstalt Fur wasserbau, Hydrologie und glaziologie. Sediment transport on steep slopes.
Takahashi, T. (1981). Debris flow. *Annual Review of Fluid Mechanics*, *13*(1), 57–77.
Tokyay, N. D., & Yildiz, D. (2007). Characteristics of free overfall for supercritical flows. *Canadian Journal of Civil Engineering*, *34*(2), 162–169.
Tsai, V. C., Minchew, B., Lamb, M. P., & Ampuero, J. P. (2012). A physical model for seismic noise generation from sediment transport in rivers. *Geophysical Research Letters*, *39*(2). L02404. https://doi.org/10.1029/2011gl050255
Ulivieri, G., Marchetti, E., Ripepe, M., Chiambretti, I., De Rosa, G., & Segor, V. (2011). Monitoring snow avalanches in Northwestern Italian Alps using an infrasound array. *Cold Regions Science and Technology*, *69*(2–3), 177–183.
Walter, F., Burtin, A., McArdell, B. W., Hovius, N., Weder, B., & Turowski, J. M. (2017). Testing seismic amplitude source location for fast debris flow detection at Illgraben, Switzerland. *Natural Hazards and Earth System Sciences*, *17*(6), 939–955.
Wang, B., Li, Y., Liu, D., & Liu, J. (2018). Debris flow density determined by grain composition. *Landslides*, *15*(6), 1205–1213.
Wenner, M., Walter, F., McArdell, B., & Farinotti, D. (2019). Deciphering debris flow seismograms at Illgraben, Switzerland. In *Association of Environmental and engineering geologists; special publication 28. Colorado school of mines*. Arthur Lakes Library.
Yamasato, H. (1997). Quantitative analysis of pyroclastic flows using infrasonic and seismic data at Unzen volcano, Japan. *Journal of Physics of the Earth*, *45*(6), 397–416.
Zhang, Z., Walter, F., McArdell, B. W., de Haas, T., Wenner, M., Chmiel, M., & He, S. (2021). Analyzing bulk flow characteristics of debris flows using their high frequency seismic signature. *Journal of Geophysical Research: Solid Earth*, *126*(12), e2021JB022755. https://doi.org/10.1029/2021jb022755
Zhang, Z., Walter, F., McArdell, B. W., Wenner, M., Chmiel, M., deHaas, T., & He, S. (2021). Insights from the particle impact model into the high frequency seismic signature of debris flows. *Geophysical Research Letters*, *48*(1), e2020GL088994. https://doi.org/10.1029/2020gl088994